



39 machinery and precursors to proliferate, the infection-to-lysis process intricately depends on  
40 the physiological characteristics of the target cell: for instance, factors such as  
41 lipopolysaccharide (LPS) composition and receptor density influence the adsorption rate<sup>3</sup>; the  
42 resources and machinery of the host cell affect the rate of virion replication<sup>4,5</sup> and the  
43 production of lytic agents necessary for cell lysis. Recent single-cell studies have unveiled  
44 significant physiological variability among genetically identical bacterial cells, raising questions  
45 about how this diversity impacts the kinetics of phage infection and how the variability in  
46 infection kinetics, in turn, influences the overall effectiveness of phages in eliminating their  
47 target bacteria at a population level<sup>6</sup>.

48  
49 The vast majority of current methods used to study the kinetics of phage infections steps in  
50 bacteria rely on bulk culture approaches and omics analysis<sup>7-9</sup>, which lack the necessary  
51 single-cell resolution to analyse cell-to-cell heterogeneity, or on cryo-EM imaging for high-  
52 resolution investigation of structural aspects, which lacks time-resolved information to monitor  
53 the progress of individual infection steps and their interrelations<sup>10,11</sup>. Recent single-cell studies  
54 have revealed unprecedented insights into the mechanisms underlying the lytic-lysogenic  
55 switch of temperate phages<sup>12</sup>. However, few studies have attempted to analyse lytic phage  
56 infection at single-cell level and to understand how the physiological diversity of host cells  
57 influences the infection cycle<sup>13,14</sup>. To achieve this, a method is needed that can: (i) precisely  
58 track each stage of infection initiated by a single phage targeting a solitary living bacterium in  
59 a time-resolved fashion, (ii) maintain a spatiotemporally homogeneous environment to isolate  
60 the impact of intrinsic variations in host cell physiology on infection parameters, and (iii) be  
61 sufficiently high throughput for quantifying the detailed distribution across these target  
62 bacterial cells.

63  
64 Here, we present an innovative approach tailored to address these challenges. Our method  
65 harnesses a microfluidic platform engineered to maintain isolated populations of target cells  
66 under uniform growth conditions, to enable the tracking of infection dynamics as individual  
67 cells become infected and lysed by individual phages. Using high-speed scanning time-  
68 resolved microscopy<sup>15</sup>, and a combination of fluorescent markers on the model system of  
69 phage T7, we are able to follow individual infection events from phage adsorption to cell lysis  
70 on individual cells of *Escherichia coli*. Altogether, the method provides the first quantification  
71 of the timing and variability in the kinetics of lytic phage infection steps. Moreover, employing  
72 this method allows us to correlate the observed fluctuations in infection parameters with the  
73 physiological parameters of the host, thereby elucidating the source of such variations.

74  
75 Analysis of these comprehensive datasets has yielded unprecedented insights into the  
76 temporal dynamics and variability of each infection stage, revealing their detailed distributions,  
77 interrelationships, and broader implications in terms of selective pressure on phage  
78 populations. Results from our simulations show that the details of the distribution of these  
79 kinetic parameters are crucial in determining the competitive fitness of a lytic phage,  
80 suggesting that variability in the phage life history parameters could constitute an evolutionary  
81 trait that is currently under-explored. Looking forward, we anticipate that our method will offer  
82 the opportunity to quantify the distribution of infection parameters, revealing an understanding  
83 of phage-bacteria interactions and their evolution previously unattainable.

84

## 85 Results

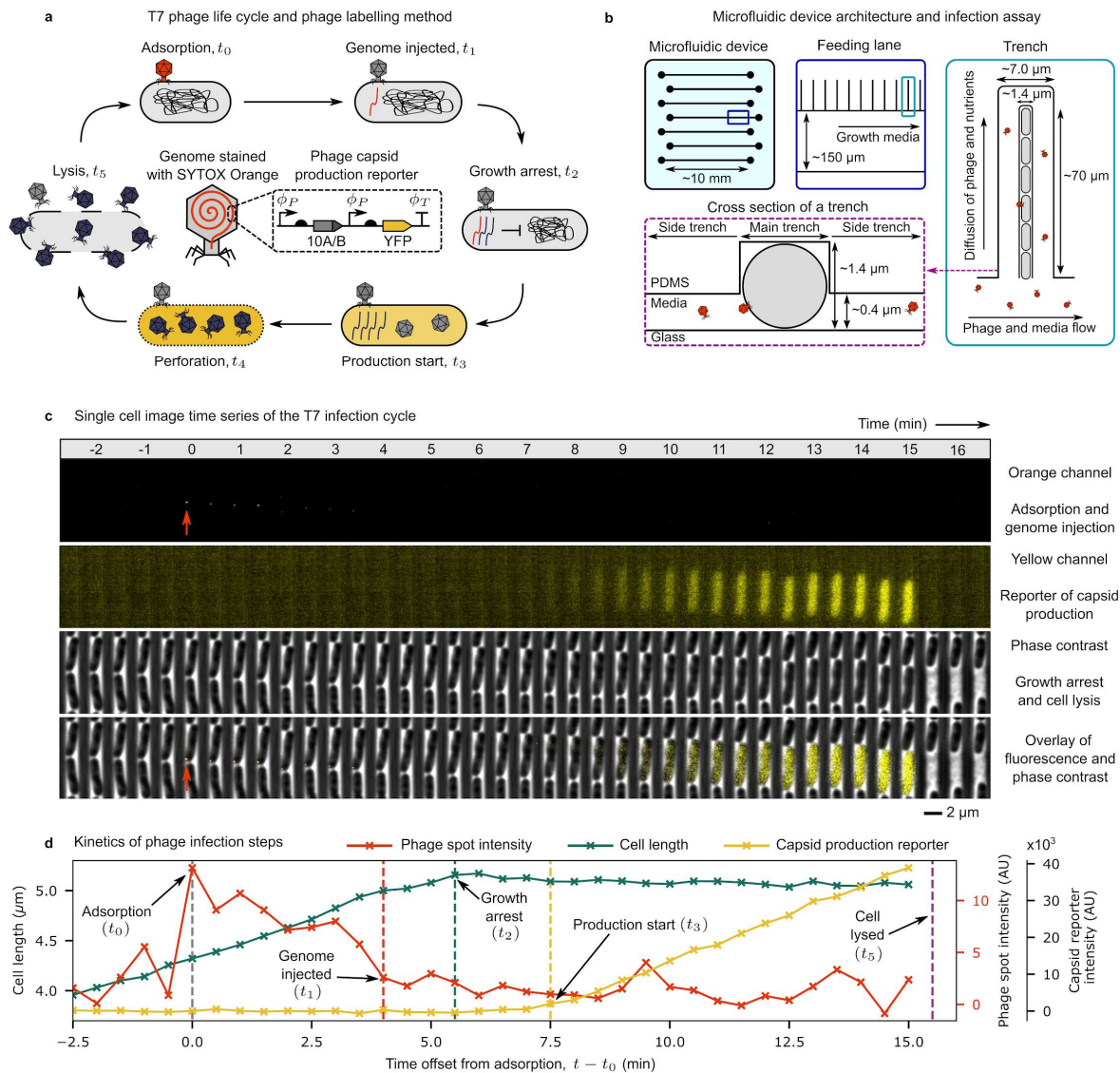
### 86 Single cell imaging of the T7 phage infection cycle

87 To identify and monitor the timing of the different steps in the T7 life cycle using fluorescence  
88 microscopy, we introduced two fluorescent labels in the phage (Fig. 1a). First, we modified the  
89 wild-type T7 genome to include a fluorescent reporter of capsid gene expression (gp10A-B,  
90 Methods, Supplementary note 1). The capsid genes are among the most highly expressed T7  
91 genes<sup>16</sup>, making them an excellent target to obtain a strong fluorescent signal for phage  
92 transcription. mVenus NB, a yellow fluorescent protein (YFP) with a very fast maturation time  
93 (4 min)<sup>17</sup>, was selected as suitable fluorescent reporter given the short phage life cycle (15-20  
94 min)<sup>18</sup>. This modified T7 phage (referred to as T7\*) was then stained with a DNA binding dye,  
95 SYTOX Orange (Fig. 1a, Methods, Supplementary note 2), to visualise phage adsorption to  
96 the host cell ( $t_0$ ) and subsequent genome injection. SYTOX Orange is spectrally compatible  
97 with the YFP reporter, has been previously used for labelling lambda phage genome<sup>19</sup> and  
98 does not affect cell growth<sup>20</sup>.

99  
100 Individual phage infection cycles in single bacterial cells (*E. coli* MG1655 7740  $\Delta$ motA) were  
101 monitored using a modified version of the 'mother machine' microfluidic device<sup>21</sup>. In this device,  
102 cells are cultivated in linear colonies within narrow (1.4  $\mu$ m wide) trenches, receiving nutrients  
103 diffusively from the media flowing through the orthogonal flow channel (Fig. 1b). In contrast to  
104 the regular mother machine design<sup>22</sup>, the narrow trenches are flanked by shallow side  
105 trenches that facilitate the diffusion of both nutrients and phage along the length of the trench<sup>21</sup>.  
106 We found that the presence of side trenches is essential for phages to infect cells deeper in  
107 the trench, so that infection events can be monitored over time all the way to lysis before the  
108 corresponding infected cell is pushed out of the trench by the replicating cells above  
109 (Supplementary note 3). As individual lineages are isolated in their own trenches and the  
110 media continuously flows throughout the experiment, the device maintains cells in a  
111 spatiotemporally uniform environment. This uniformity is key to minimise potential sources of  
112 heterogeneity arising from a variable environment and truly quantify the stochasticity of  
113 individual steps in the infection process across a bacterial population experiencing identical  
114 external conditions. Additionally, as we operate at very low multiplicity of infection, we can  
115 ensure that the first lysis events in each trench are truly originating from the infection of one  
116 bacterium by one single phage, as evidenced by the rare occurrences of such events  
117 (Supplementary movie 1).

118  
119 The cells are loaded into the device and grown in LB Miller with pluronic for a minimum of  
120 three hours to allow them to reach a steady-state exponential growth phase. Subsequently,  
121 the media is switched to media with added phage (Methods). High-speed time-resolved  
122 scanning microscopy<sup>15</sup> was used to collect multichannel data at high time-resolution (2 frames  
123  $\text{min}^{-1}$ ) during the infection events (Supplementary movie 2) and processed using a machine-  
124 learning model trained with synthetic micrographs<sup>23</sup> (Methods, Supplementary note 4), to  
125 quantify cell physiology and infection markers over time. Individual infected cells were tracked  
126 across frames using a custom-designed lineage-tracking algorithm, which accommodates the  
127 disappearance of a subset of cells due to phage-induced lysis (Supplementary note 5). An  
128 example of a resultant multichannel kymograph of a single infection event is shown in Fig. 1c  
129 and its corresponding time-series data in Fig. 1d. In the orange channel, the adsorption of the

130 SYTOX Orange stained phage to a cell is seen as an orange dot ( $t_0$ ), which fades and  
 131 disappears over time as the genome is injected ( $t_1$ ). In the yellow channel, the YFP signal of  
 132 the capsid production reporter can be seen increasing in intensity ( $t_3$ ) after genome injection  
 133 is completed and up to cell lysis. The phase contrast channel shows cell growth up until a  
 134 point, post-phage-adsorption, when the growth in length stops abruptly ( $t_2$ ), and the cell  
 135 eventually lyses ( $t_5$ ). In the following sections, we analyse the heterogeneity of each of these  
 136 steps across different infection events.  
 137



138  
 139 **Fig. 1: An assay for imaging the T7 phage infection cycle at the single-cell level**  
 140 **a.** An overview of six key time points in the T7 life cycle, which we use throughout the study  
 141 to quantify the kinetics of infection steps in the phage life cycle. The DNA staining method and  
 142 genomic location of the capsid production reporter are indicated in the centre of the loop. **b.** A  
 143 description of the microfluidic device and infection assay used in this study. **c.** Kymographs  
 144 showing a T7\* phage (indicated by the red arrow) infecting a single bacterial cell. The orange  
 145 channel image has been bandpass filtered to remove bleedthrough from the YFP capsid  
 146 production reporter (Supplementary note 6). **d.** Time series data corresponding to the phage  
 147 infection images presented in (c) demonstrate the typical progression of signals during T7\*

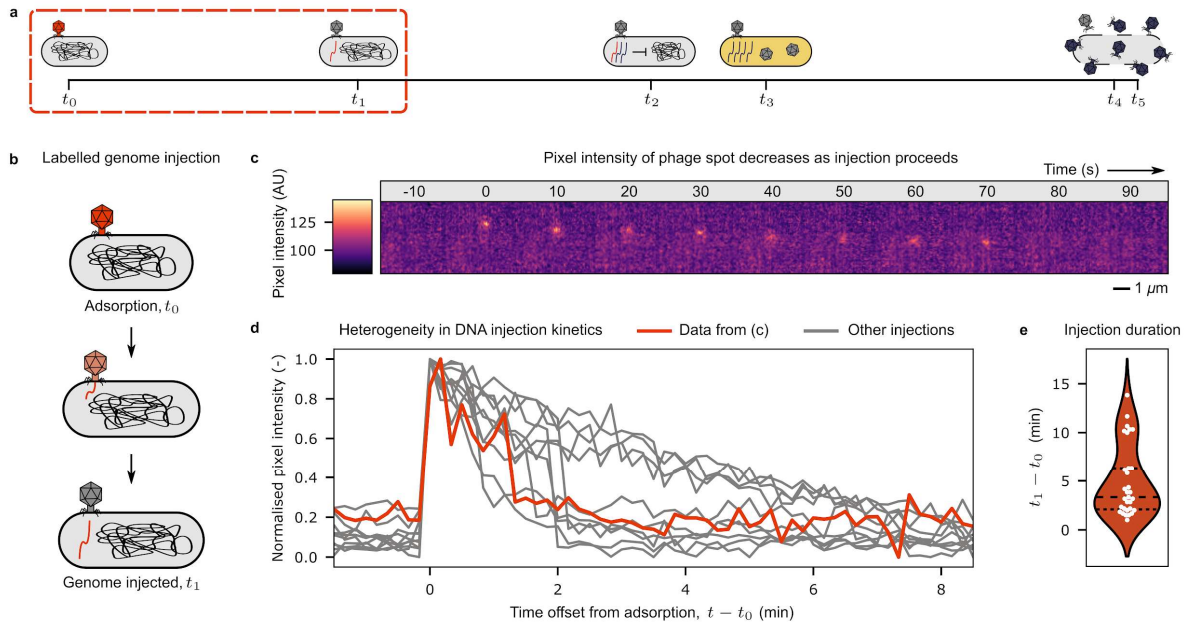
148 infection. With the exception of perforation, which happens very close to lysis, all time points  
149 from Fig. 1a are labelled on the time series.

## 150 Genome injection kinetics show two distinct entry modalities

151 The molecular mechanisms that lead to T7 genome entry have been extensively studied<sup>24–27</sup>  
152 and result in a three-step process: (i) up to the first 850 base-pairs<sup>28</sup> enter the cell as the phage  
153 tail penetrates the cell wall and membrane, (ii) the host RNA polymerase (RNAP) recognises  
154 a series of binding sites on the genome and translocates it while transcribing the early genes,  
155 including the T7 RNAP, (iii) once expressed, the T7 RNAP takes over the process and pulls  
156 in the remaining 85% of the genome.

157  
158 Studies in bulk cultures have shown that the whole process takes approximately 4 minutes on  
159 average<sup>28,29</sup>, however, the variability of its dynamics within a population is unknown. In our  
160 setup, we can track such dynamics across multiple infection events, by quantifying the  
161 fluorescence signal coming from the labelled phage DNA over time (Fig. 2, Methods,  
162 Supplementary note 7). When the phage binds to a cell, a bright spot suddenly appears in the  
163 orange channel due to the immobilisation of the phage upon adsorption (Fig. 2c). The  
164 fluorescence intensity of the spot then decreases over time as the genome gradually leaves  
165 the viral capsid and enters the cell (Supplementary movie 3).

166  
167 Across multiple adsorption events, we observed significant heterogeneity in the progression  
168 of genome injection (Fig. 2d-e). The intensity trends reveal two broad classes of entry  
169 dynamics. In one, the injection progresses steadily to completion at an approximate rate of 4  
170 kbps min<sup>-1</sup> (Supplementary note 8). In the other, the entry proceeds similarly up to  
171 approximately 1.5 min, but then a sudden transition occurs in which the rest of the genome  
172 quickly enters the cell. These results suggest two potential modes of entry. The first class of  
173 trajectories would be consistent with the host RNAP being responsible for translocating the  
174 whole phage genome into the cell (*E. coli* RNAP's transcription velocity is between 1.2 and  
175 5.4 kbps min<sup>-1</sup>)<sup>30</sup>. The second class aligns with the established three-step genome entry  
176 process, in which the first 6 kbps of the phage genome are translocated by the host RNAP  
177 and the rest by the much faster T7 RNAP. The distribution of the injection time duration (Fig.  
178 2e) displays a mean duration time of 4.9 min, consistent with previous bulk experiments, with  
179 a large variability across infection events (coefficient of variation (CV) = 74%, n = 31). This  
180 large variability could be explained by the observed bimodality of the process in which  
181 approximately one third of the injection events belong to the first class, and two thirds to the  
182 second.



183

184

## Fig. 2: Heterogeneity in phage genome injection kinetics

185

**a.** A timeline showing the temporal location of genome injection in the T7 life cycle. **b.** A schematic of T7 genome injection. **c.** A kymograph of genome injection shown as a heat map.

186

The phage spot moves vertically downwards in sequential frames due to cell growth. **d.** A comparison of phage spot intensities over time for several genome injection events. Signals have been background corrected and normalised. The injection shown in (c) is displayed in orange and examples of ten other injections are displayed in grey.

187

**e.** A violin plot showing the distribution of genome injection durations ( $t_0$  to  $t_1$ ). The central dashed line represents the median and the outer dashed lines the first and third quartiles. The mean injection duration is 4.9 min ( $n = 31$ ,  $CV = 74\%$ ).

188

189

190

191

192

193

194

## Kinetics of host cell shutdown and viral takeover are

195

## remarkably consistent across infection events

196

The T7 early (class I) genes, transcribed at the beginning of the infection process by the host RNAP, are responsible for the shutdown of the host cell, including the inhibition of cell wall synthesis<sup>31,32</sup>. We therefore expect cell growth arrest to be among the first signs that phage proteins are being produced. Our fluorescent transcriptional reporter for the capsid proteins, in addition, pinpoints the onset of expression of late (class III) genes from the phage genome.

197

Together, these two markers (growth arrest and capsid expression reporter) allow us to analyse the kinetics and variability in phage protein production during the infection process (Fig. 3a).

198

199

200

201

202

203

204

A representative time series from a single infection event is illustrated in Fig. 3b. The green line depicts cell length,  $L(t)$ , where the abrupt periodic drops prior to infection correspond to cell division events. The instantaneous growth rate for each cell,  $\lambda$ , is calculated from the local slope of the  $\ln(L(t))$  time series (Fig. 3c, Supplementary note 9). The precise moment of growth arrest ( $t_2$ ) is determined when the instantaneous growth rate falls below a given threshold (Supplementary note 9). Soon after growth arrest is detected, we observe the level of capsid expression ( $I(t)$ , yellow line) to increase rapidly until lysis occurs (Fig. 3b).

205

206

207

208

209

210

211

212

213 Growth arrest dynamics are found to be remarkably robust across different infection events  
214 (Fig. 3c). Cells transition from pre-infection growth rates to complete cessation within 3-4 min  
215 and in a consistent fashion, independently of their size or position in the cell-cycle. By contrast,  
216 expression of the capsid reporter displays considerable variability (Fig. 3d), with the maximum  
217 intensity of the reporter,  $I_{max}$ , varying by almost an order of magnitude across infection events.  
218 We found the variability in  $I_{max}$  to be strongly correlated with the size of the growth arrested  
219 cell ( $L_{GA}$ ) (Fig. 3d, right). Larger production rates in larger cells would be consistent with the  
220 presence of more ribosomes, which is likely the limiting factor in phage protein production. We  
221 investigate this in the next section.

222

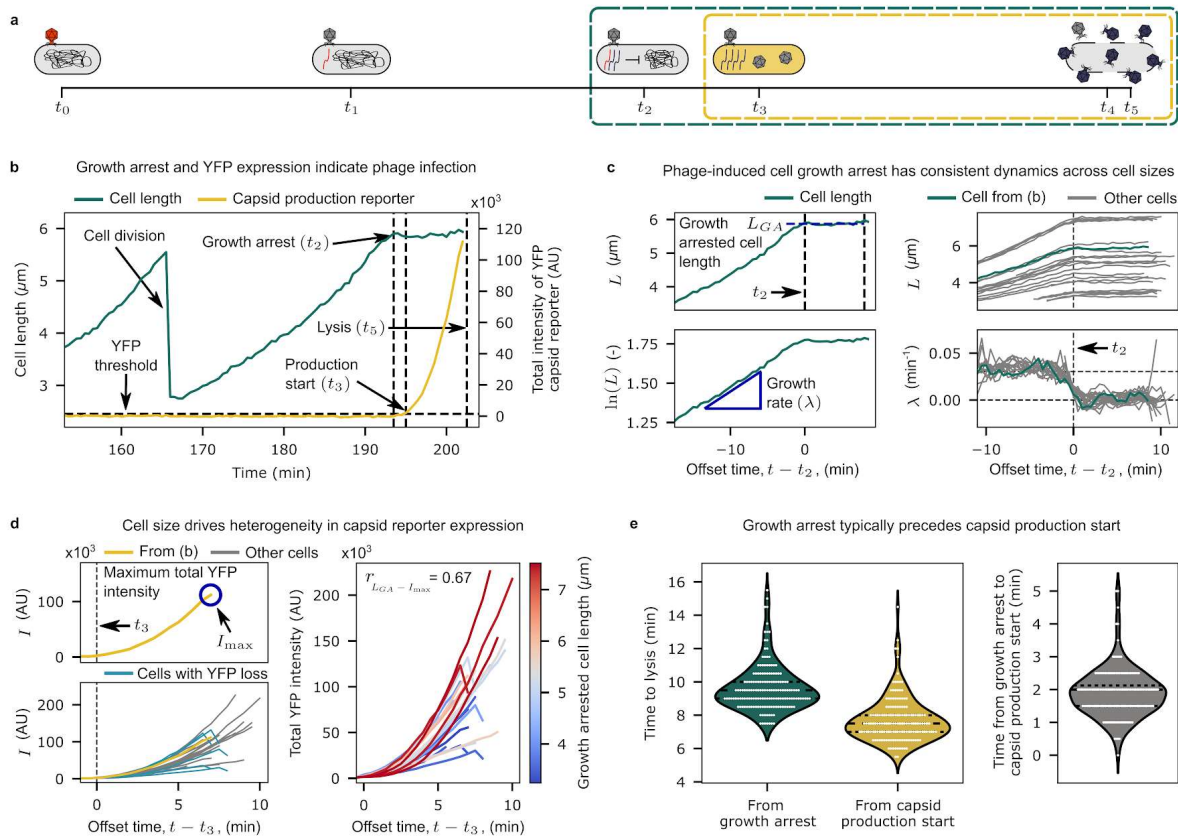
223 In five of the 23 example infections presented in Fig. 3d, the YFP intensity sharply decreases  
224 in the final observation before lysis (highlighted in green, Fig. 3d). This decline in signal  
225 coincides with the perforation of the cell envelope ( $t_4$ , detailed in Fig. 5 and Supplementary  
226 note 10).

227

228 Unlike the genome injection process discussed earlier ( $t_0$  to  $t_1$ ), the time intervals between  
229 growth arrest and subsequent lysis ( $t_2$  to  $t_5$ ) and between start of capsid production and lysis  
230 ( $t_3$  to  $t_5$ ) are narrowly distributed (respectively, CV of 15% and 17%, Fig. 3e), with the latter  
231 delayed on average by 1.9 min compared to the first. We note here that the folding and  
232 maturation of the reporter proteins can take minutes, implying that actual expression of the  
233 capsid genes might start at the same time, if not earlier than the growth halt of the host cell.  
234 Taken together, these results suggest that once the phage has taken control over the cell, the  
235 timing of events proceeds almost deterministically.

236

237



238

239

240

241

242

243

244

245

246

247

248

249

250

251

252

253

254

255

256

257

258

259

260

261

262

**Fig. 3: Kinetics of host shutdown and phage gene expression**

**a.** A timeline showing the temporal location of growth arrest and capsid production start in the T7 life cycle. **b.** Example time series data showing representative cell length and capsid reporter expression data of a cell which becomes infected. Three time points, the growth arrest ( $t_2$ ), capsid production start ( $t_3$ ) and lysis ( $t_5$ ), are indicated. The threshold intensity used to define production start is also indicated. **c.** We use the growth arrested cell length as a measure of cell size after host takeover (left, top panel). The cell growth rate is calculated as the instantaneous slope of the natural log-transformed cell length (left, bottom panel). Comparison of the cell length (right, top panel) and growth rate (right, bottom panel) between the cell in panel (b) (green lines) and 22 other infected cells (grey lines). The growth arrest kinetic is highly consistent between cells. **d.** Capsid reporter production is highly variable between different infection events. We use total YFP intensity summed over the cell,  $I$ , as a measure of capsid reporter production, and hence the maximum total YFP intensity,  $I_{max}$ , (left, top panel) as a proxy for the total number of capsid proteins produced in a cell. Example data from 23 infection events (left, bottom panel) shows the variability in capsid reporter production kinetics, comparing the example from panel (b) (yellow line) to other events (grey lines). Five events are highlighted in green; these cells show a sharp drop in YFP signal in the final observation before lysis due to the perforation of the cell envelope (see Supplementary note 10). The variability in production kinetics is linked to differences in cell size (right). The lines are coloured by the growth arrested cell length of each cell and the maximum total YFP intensity is positively correlated with the growth arrested cell length ( $r = 0.67$ ). **e.** Growth arrest typically precedes production start by a mean time delay of 1.9 min. The violin plots show kernel density estimates of the timings from growth arrest (green) and production start (yellow) to lysis, along with the timings between growth arrest and production start (grey). The central

263 dashed line represents the median and the outer dashed lines the first and third quartiles. The  
264 mean time from growth arrest to lysis ( $t_2$  to  $t_5$ ) is 9.6 min ( $n = 166$ ,  $CV = 15\%$ ). The mean time  
265 from production start to lysis ( $t_3$  to  $t_5$ ) is 7.7 min ( $n = 160$ ,  $CV = 17\%$ ). The mean time from  
266 growth arrest to production start ( $t_2$  to  $t_3$ ) is 1.9 min ( $n = 160$ ,  $CV = 39\%$ ).  
267

## 268 Phage protein production kinetics are strongly coupled with the 269 physiological variability of the host

270  
271 The observed high variability in protein production, despite the remarkable robustness of  
272 timing of events, hints to other sources of heterogeneity beyond production time. To  
273 understand the source of this heterogeneity and its correlation with the cell size at the moment  
274 of growth arrest,  $L_{GA}$  (Fig. 3d), we developed a mathematical model that takes into account  
275 viral genome replication, transcription, and translation (Fig. 4a, details in Supplementary note  
276 11). In brief, the model assumes that the phage genome replication is autocatalytic, and the  
277 genome replicates exponentially with a rate  $\lambda_1$ . If the number of genome copies and not T7  
278 RNAP is the limiting factor in transcription, this leads to an exponentially growing amount of  
279 mRNA encoding YFP. The translation rate, and thus YFP production, depends on the available  
280 number of mRNA copies,  $m$ , and the number of ribosomes present in the cell according to a  
281 simple Hill equation (Fig. 4a, Supplementary note 11). The maximum translation rate,  $\lambda_2$ , is  
282 then a proxy for the total number of ribosomes in the cell.  
283

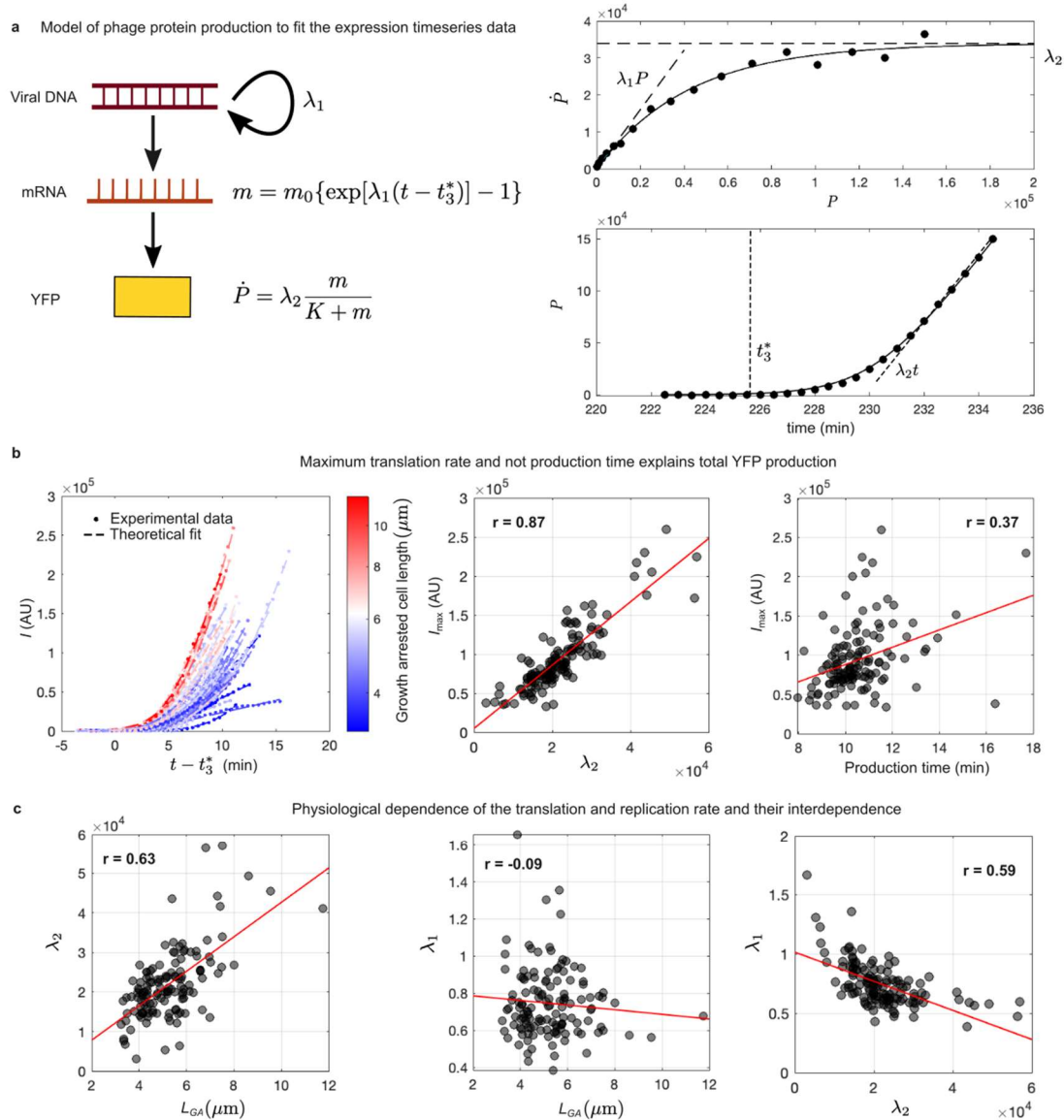
284 The dynamics of YFP can be solved analytically, providing simple functional forms for  $dYFP/dt$   
285 as a function of YFP and of YFP as a function of time:

$$287 \quad dYFP/dt = \lambda_2[1 - \exp(-\lambda_1/\lambda_2 YFP)], \quad (1)$$

$$288 \quad YFP = \lambda_2/\lambda_1 \log\{1 + \{\exp[\lambda_1(t - t_3^*)] - 1\}/K_0\}, \quad (2)$$

289  
290 where  $K_0 = K/m_0$  (Fig. 4a and Supplementary note 11).

291 These allow us to estimate the model parameters from the experimental fluorescence intensity  
292 time series (Fig. 4a, Supplementary note 11). By fitting each cell's time series, we can extract  
293 values for  $\lambda_1$ ,  $\lambda_2$  (from eq. 1), and the time,  $t_3^*$  (from eq. 2) at which protein production starts  
294 (Fig. 4b). We find that the maximum translation rate,  $\lambda_2$ , strongly correlates with maximum  
295 YFP values, pointing at the number of ribosomes in the infected cell as the key variable  
296 controlling phage protein production (Fig. 4b). By contrast, production time, defined as  $t_5 -$   
297  $t_3^*$ , shows only a weak correlation with maximum YFP, in line with the idea that the major  
298 source of variability in phage protein production lies in the number of ribosomes of the infected  
299 cell and, therefore, the cell's physiological state at the time of viral takeover, and not the latent  
300 period of infection, as previously thought<sup>33-35</sup>.



301  
302

#### Fig. 4: Maximum translation capacity explains phage protein production

303 **a.** Schematic diagram of the mathematical model for phage protein production from viral  
 304 genome duplication, through gene transcription to protein translation. The two analytical  
 305 functions,  $dP/dt$  as a function of  $P$  (eq. 1) and  $P$  as a function of time (eq. 2) are sequentially  
 306 used to fit the experimental data and determine  $\lambda_1$ ,  $\lambda_2$ , and production start time,  $t_3^*$ . **b.** Time-  
 307 series data of YFP expression are shifted to align production start time ( $t_3^*$ ), with traces  
 308 coloured according to cell length at growth arrest. The maximum YFP signal observed,  $I_{max}$ ,  
 309 strongly correlates with the inferred maximum translation rate  $\lambda_2$ , and only moderately with  
 310 inferred production time ( $t_3^*$  to  $t_5$ ). **c.** Maximum translation rate correlates with cell length at  
 311 growth arrest ( $L_{GA}$ ), linking cell physiology with this parameter. By contrast, phage genome  
 312 duplication rate,  $\lambda_1$ , shows no correlation with host cell features (Supplementary note 11).  
 313 Intriguingly,  $\lambda_1$  and  $\lambda_2$  show a negative correlation.  
 314

315  
316

317 Unsurprisingly, we find that  $\lambda_2$  positively correlates with cell size at the point of growth arrest  
 318 (Fig. 4c), which explains the empirical correlation between maximum YFP and cell size in the

319 experimental data (Fig. 3d). Importantly, our YFP marker was designed to track capsid protein  
320 expression and, as such, is our best proxy for the number of viral capsids produced by the  
321 infected cell, i.e., the burst size. Our results therefore suggest that burst size could, in principle,  
322 vary by almost one order of magnitude even in perfectly homogeneous conditions, simply  
323 because of physiological differences across infected cells.

324  
325 Beyond maximum YFP production, the model results reveal some additional intriguing  
326 observations. The lack of correlation between  $\lambda_1$  and any of the experimentally observed  
327 features of the infected cell (Fig. 4c and Supplementary note 11) suggests that viral genome  
328 replication and late genes transcription is independent of the host physiology, at least in these  
329 experimental settings. Surprisingly, we also observe a significant negative correlation between  
330  $\lambda_1$  and  $\lambda_2$ , suggesting the presence of a negative feedback between viral genome replication  
331 and translation. A possible explanation is that, if translation is fast, viral capsids might  
332 assemble rapidly, spooling in viral DNA and thus depleting the pool of viral genomes that could  
333 replicate. Further work is necessary to test this or alternative hypotheses.

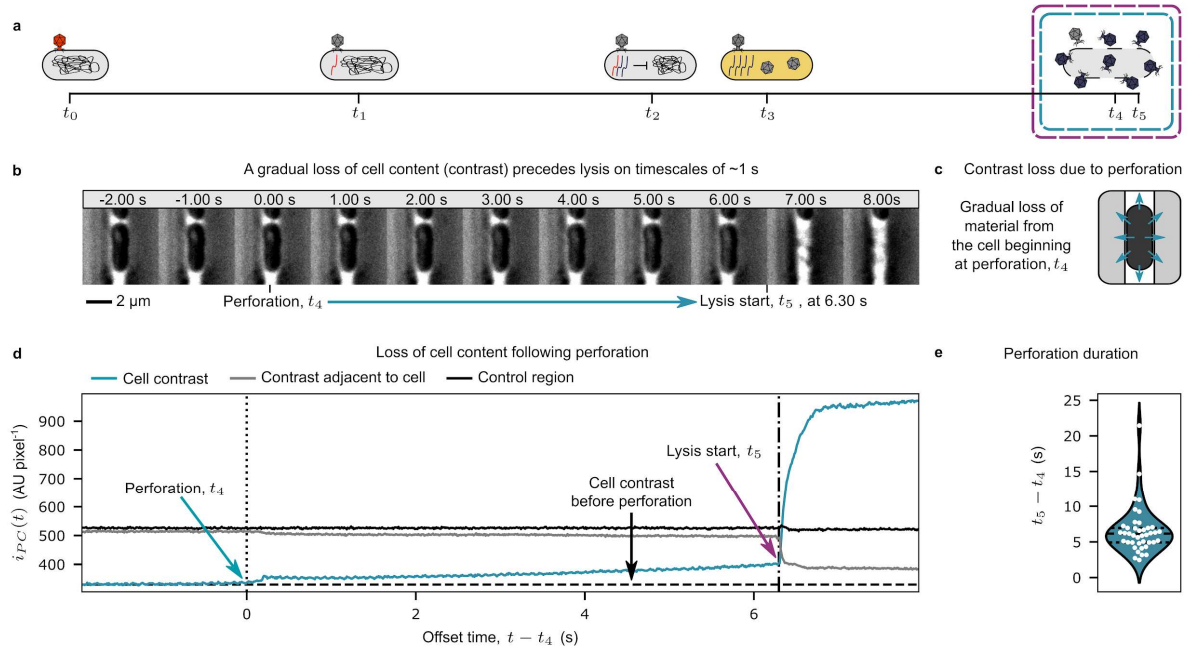
334

## 335 Gradual perforation of the cell membrane precedes the abrupt 336 lysis of the infected cell

337 The concluding stage of the infection process involves the lysis of the host cell. We collected  
338 high-frame rate images (100 Hz) to visualise the events preceding cell lysis (Methods,  
339 Supplementary movie 4). The process of lysis unfolds in two distinct phases. The initial phase,  
340 here termed as perforation, involves a gradual leakage of material from the cell, resulting in a  
341 subtle increase in phase brightness (Fig. 5b), accompanied by a gradual decrease in the  
342 intensity of the surrounding environment. This phase is slower, lasting several seconds, and  
343 typically begins with a small but sharp increase in phase brightness (Fig. 5d), marking the  
344 onset of perforation ( $t_4$ ). Material is then steadily lost from the cell until the commencement of  
345 the second phase at  $t_5$ . The subsequent phase, referred to as lysis, represents the final  
346 structural breakdown of the cell envelope. This is indicated by the rapid increase in the phase  
347 contrast intensity (purple arrow in Fig. 5d). We estimated the mean duration between the onset  
348 of perforation and the start of lysis ( $t_4$  to  $t_5$ ) to be 6.57 s.

349

350 In Fig. 3d, we observe that in some infections, the YFP signal drops in the final observation  
351 prior to lysis. This phenomenon is only observed in a fraction of the infection events due to the  
352 short interval between perforation and lysis compared to the frame rate of the images taken.  
353 With a mean perforation to lysis time of 6.57 s, we only expect to observe the drop in YFP in  
354 21.9% of infections when imaging at 2 frames  $\text{min}^{-1}$ , which is consistent with the results shown  
355 in Fig. 3d and the observed increase in phase contrast signal of those cells (indicating a loss  
356 of material from the cell) as shown in Fig. S7.



357  
358  
359  
360  
361  
362  
363  
364  
365  
366  
367  
368

**Fig. 5: A gradual loss of cell contents precedes cell lysis**

**a.** A timeline of the T7 phage life cycle, indicating the timing of perforation ( $t_4$ ) and lysis ( $t_5$ ).  
**b.** A kymograph showing the cell lysis on timescales of 1.00 s. The time axis is offset such that perforation ( $t_4$ ) starts at time zero. **c.** A schematic illustrating the gradual loss of material from the cell which follows perforation and gives a loss of contrast in the images. **d.** Time series data showing the phase contrast intensity within and outside the cell shown in the kymograph in **(b)**. **e.** Violin plot showing the distribution of perforation duration across different infection events (perforation start to lysis start,  $t_4$  to  $t_5$ ). The mean perforation duration is 6.57 s ( $n = 41$ , CV = 51%).

## 369 Heterogeneity in lysis time is driven by variability in the early 370 stages of infection

371 Having measured the timing of several points in the infection cycle, we set out to construct a  
372 full timeline of the typical T7 infection cycle, alongside a comparison of the relative  
373 contributions of each individual infection step to the overall variability in lysis time.

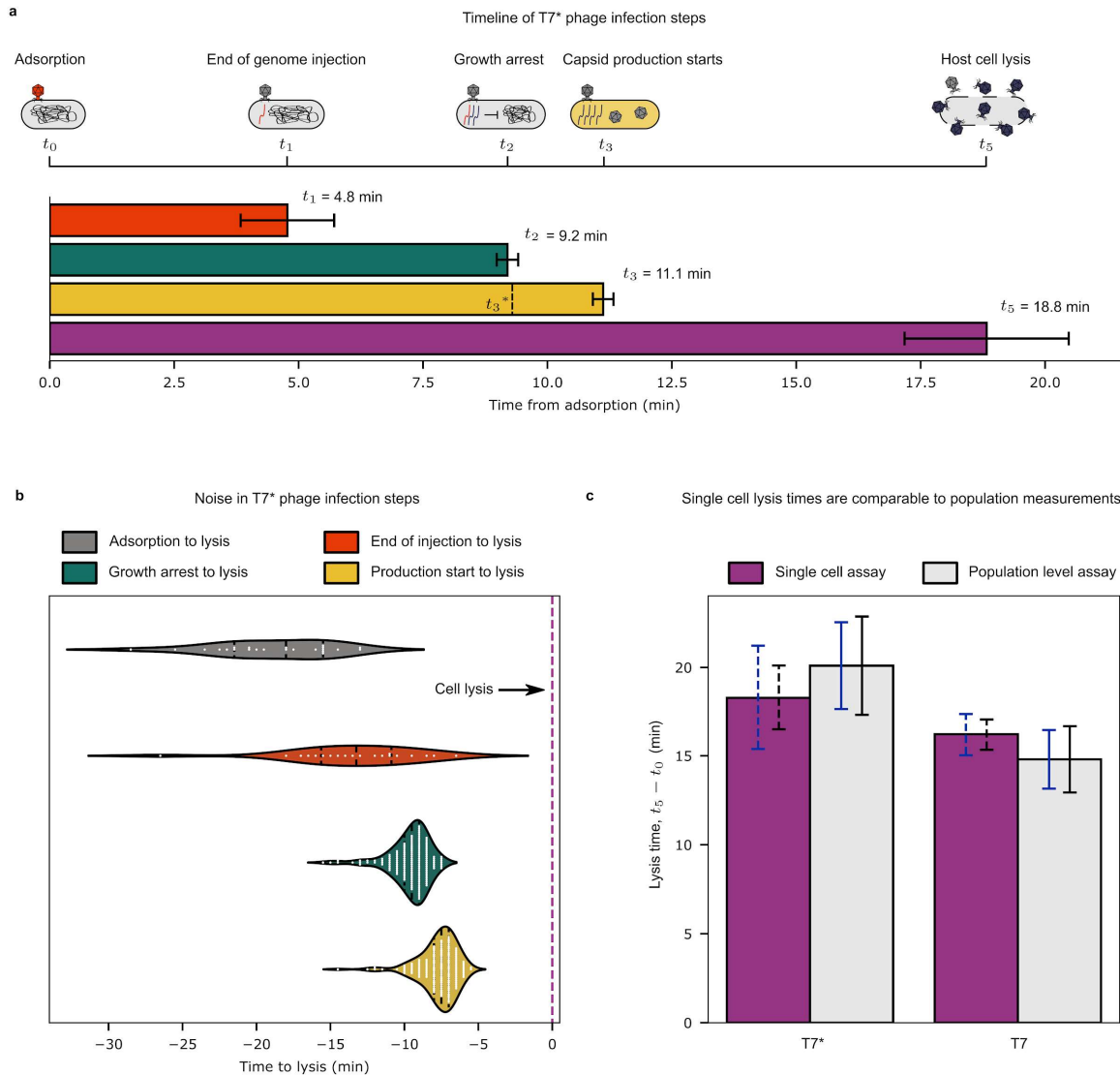
374  
375 Fig. 6a illustrates a comprehensive timeline of the typical infection cycle of T7\* on *E. coli* cells,  
376 from phage adsorption onto the cell to the mean of four key time points in the infection cycle:  
377 genome injection ( $t_1$ ), host cell shutdown ( $t_2$ ), capsid production ( $t_3$ ), and cell lysis ( $t_5$ ). Error  
378 bars accompany each time point, representing the range of variability (95% confidence  
379 interval). The perforation step ( $t_4$ ) is not represented here due to its negligible duration  
380 compared to the other stages (Fig. 5).

381  
382 Analysis of this timeline reveals that genome injection typically concludes 4.8 min after phage  
383 adsorption, accounting for just over one quarter of the overall lysis time (18.8 min).  
384 Approximately 9.2 min into the infection cycle, the host cell ceases growth, then capsid  
385 production starts at 11.1 min after adsorption. However, the adjusted production start time

386 inferred from the model ( $t_3^*$ ) is 9.3 mins after adsorption, suggesting the capsid production  
387 actually starts almost simultaneously with host takeover. Approximately 9.6 min after the host  
388 takeover (calculated as  $t_5 - t_2$ ), the cell undergoes lysis, releasing the phage copies into the  
389 surrounding environment. The average duration from adsorption to lysis, the lysis time, is  $18.8$   
390  $\pm 1.6$  min for T7\*, consistent with the value obtained from bulk experiments ( $20.1 \pm 2.7$  min,  $n$   
391  $= 3$ , Fig. 6c, Supplementary note 12). For wild type T7 phage without the genomically  
392 integrated capsid expression reporter, we estimated the average time between adsorption and  
393 lysis to be  $16.2 \pm 0.9$  min, also consistent with the corresponding bulk average ( $14.8 \pm 1.9$  min,  
394  $n = 3$ , Fig. 6c). The observed difference in lysis time between the two strains could be  
395 explained by the additional burden imposed by the expression of the capsid reporter.

396

397 Our results show that the lysis time exhibits a CV of 21% across infection events. Fig. 6b  
398 illustrates the contribution of each step in the infection cycle towards this variability. Here, all  
399 time points are directly measured with reference to cell lysis, as this is the most sudden and  
400 clearly identifiable of the events. We find that the variability in the overall lysis time is  
401 comparable to the variability in the time interval between the end of injection ( $t_1$ ) and lysis ( $t_5$ ).  
402 Conversely, both the durations between growth arrest and lysis ( $t_2$  to  $t_5$ ), and capsid  
403 production start and lysis ( $t_3$  and  $t_5$ ), are very consistent, with interquartile ranges spanning  
404 just 1.5 min (<10% of the lysis time). These data suggest that the primary sources of variability  
405 in lysis time stem from the initial stages of infection up to the point in which cell growth stops.  
406 After this point, which delineates the time when the phage has likely taken control of the host  
407 cellular machinery, the timing of events is remarkably consistent across infection events.



408  
409  
410

**Fig. 6: The timing of individual steps of infection and the associated variability across events**

411 **a.** Timeline of phage infection steps. Each bar represents the mean time from adsorption to  
412 the indicated time point in the T7\* phage life cycle. The adjusted production start time from  
413 the model results in Fig. 4,  $t_3^*$ , is indicated as a dashed line on the yellow bar. The error bars  
414 represent a 95% confidence interval. The data is pooled from three single cell experiments,  
415 giving total sample sizes for the measurement of  $t_1$  (injection end),  $t_2$  (growth arrest),  $t_3$   
416 (production start) and  $t_5$  (lysis) of 20, 166, 160 and 23, respectively. **b.** Kernel density  
417 estimates of the timing distributions from different time points in the T7\* phage life cycle to  
418 lysis. Each single-cell infection event measured is shown as a white dot. Inner and outer  
419 dashed lines in each violin represent the median and lower and upper quartiles respectively.  
420 Adsorption to lysis (grey violin) has mean 18.8 min, CV = 21%, n = 23. Injection end to lysis  
421 (orange violin) has mean 13.4 min, CV = 33%, n = 20. Growth arrest to lysis (green violin) has  
422 mean 9.6 min, CV = 15%, n = 166. Production start to lysis (yellow violin) has mean 7.7 min,  
423 CV = 17%, n = 160. The perforation to lysis time is not included, as relative to the timescales  
424 of the other steps, the contributed noise from this step is negligible (the mean is 6.57 s, CV =  
425 51%, n = 41). **c.** Lysis times measured with single-cell and population level methods are  
426 comparable. Purple bars represent the mean of single-cell lysis times from one experiment,

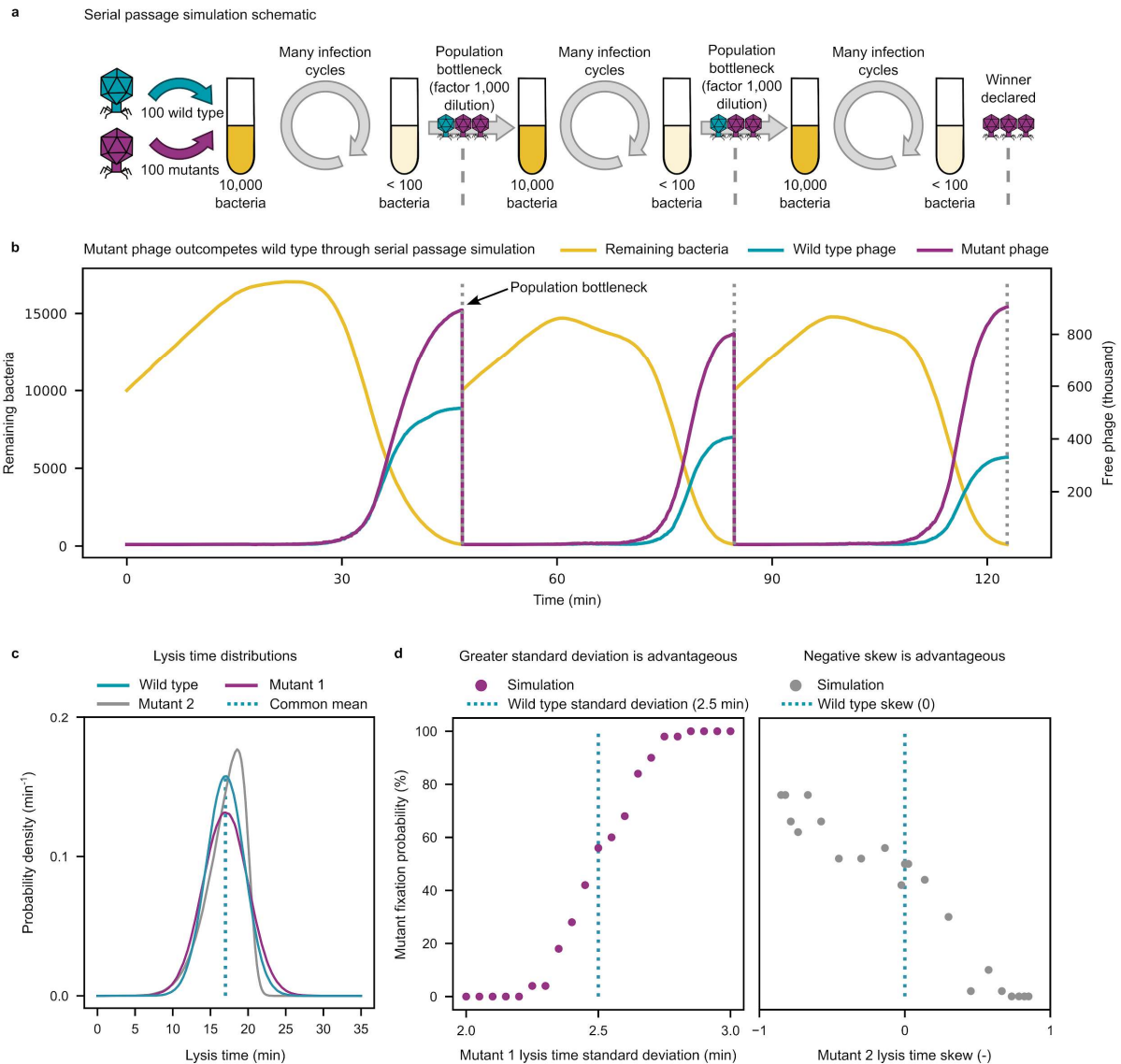
427 and grey bars represent the mean of three population level lysis time measurements (three  
428 biological replicates). Accordingly, dashed error bars are calculated from single-cell data as  
429 described, and solid error bars are calculated from biological replicates of population level  
430 assays. The blue error bars represent  $\pm 1$  standard deviation, and the black error bars  
431 represent the 95% confidence interval. The mean lysis times of T7\* obtained from single-cell  
432 and population level measurements (18.3 min,  $n = 10$  and 20.1 min,  $n = 3$  respectively) are  
433 not significantly different when compared with a t-test. The mean lysis times of T7 obtained  
434 from single-cell and population level measurements (16.2 min,  $n = 7$  and 14.8 min,  $n = 3$   
435 respectively) are also not significantly different when compared with a t-test. For all data in  
436 Fig. 6, events with a lysis time of 30 min or more are treated as outliers and excluded from the  
437 distribution. More detail on the single-cell selection criteria is given in Supplementary note 13.

## 438 Lysis time variability can provide fitness advantages to phage 439 populations

440 Lysis time represents a key life history parameter for lytic phages and is known to be under  
441 strong selective pressure in laboratory experiments<sup>36-40</sup> and potentially in the wild. Its fitness  
442 effect on phage populations in different environments is theoretically well studied, however,  
443 due to the lack of experimental data regarding its level of stochasticity, it is typically assumed  
444 to be either noiseless or exponentially distributed for modelling convenience<sup>41-44</sup>. Our data  
445 provide the unprecedented opportunity to quantify lysis time variability, raising the question of  
446 whether it can represent an evolutionary trait conferring a fitness advantage to a phage  
447 population.

448  
449 To investigate this question, we used stochastic agent-based simulations of a serial passage  
450 experiment, in which two phage populations, denoted as “wild type” and “mutant”, are initially  
451 mixed in equal proportion and then passaged through several population bottlenecks until one  
452 phage approaches fixation (Fig. 7a, Methods, Supplementary note 14). The wild type and  
453 mutant phage share the same burst size distribution, but have distinct and inheritable lysis  
454 time distributions. Some examples of these distributions are shown in Fig. 7c. Mutant 1 has  
455 the same mean lysis time as the wild type, but different standard deviation. Mutant 2 has the  
456 same mean and standard deviation in lysis time as the wild type, but different skew.

457  
458 Fig. 7d shows the probability of mutant fixation as a function of standard deviation (mutant 1,  
459 left panel) and skew (mutant 2, right panel) determined over 25 independent simulations. The  
460 results show that a larger standard deviation confers a fitness advantage, if mean and skew  
461 are the same, while a negative skew in lysis time is advantageous when the mean and  
462 standard deviation are the same. Overall, our results clearly indicate that the mean lysis time  
463 alone is not sufficient to predict phage fitness, and the higher order moments of the distribution  
464 can significantly alter a phage’s competitive advantage. We note that, although here we  
465 investigate the effect of variation in lysis time, while keeping the other phage life history  
466 parameters constant, in reality, these parameters are likely dependent on each other, giving  
467 rise to a range of tradeoffs. Future work will explore how such inter-dependencies in variability  
468 can shape phage fitness.



469

470

**Fig. 7: Simulations predict lysis time variance and skewness impact phage fitness**

471

**a.** A schematic explaining the serial passage simulation, where a wild type and mutant phage

472

with corresponding lysis times drawn from different distributions (Fig. 7c) compete and

473

undergo several rounds of dilution into fresh bacteria (Methods, Supplementary note 14). **b.**

474

Example time series data from the simulations, demonstrating the growth and lysis of the

475

bacteria (yellow line), and the proliferation of the wild type and mutant phage (blue and purple

476

lines respectively). At the population bottleneck, a 1000 fold dilution of the phage into fresh

477

bacteria is simulated. If, after a bottleneck, one phage accounts for more than 70% of the total

478

phage population, it is declared the winner. **c.** Example lysis time distributions of wild type and

479

mutant phage. Mutant 1 (purple) has the same mean as the wild type (blue), but the standard

480

deviation in lysis time is varied (Fig. 7d, left panel). Mutant 2 (grey) has the same mean and

481

standard deviation as the wild type, but the skew in lysis time is varied (Fig. 7d, right panel).

482

**d.** When competing against a wild type phage, mutants with lysis times drawn from a

483

distribution with equal mean but greater variance are predicted to have a fitness advantage

484

(left panel). Mutants with lysis times drawn from a distribution with equal mean and variance to

485

the wild type but with negative skew are also predicted to have a fitness advantage (right

486

panel). Each data point is computed from 25 simulations.

## 487 Discussion

488 Here, we have reported the first study that quantifies the kinetics of individual steps in the lytic  
489 cycle of phage T7 at single phage-single cell resolution. Our novel assay provides a new way  
490 to quantify phage-bacteria interactions that is orthogonal to omics analyses, which provide  
491 dynamic but averaged phenotypes, and structural investigation, which assess variability but  
492 are based on static observations. Our approach enables dynamic measurements across many  
493 infection events in a precisely controlled environment, while maintaining the individuality of  
494 each of them in order to assess variability and correlations across the phenotypes of the phage  
495 and the corresponding infected cell.

496  
497 We find that the major source of variability in the timing of infection events comes from the  
498 early steps of viral DNA entry up to cell growth arrest, while the second part of the infection  
499 process, between host take-over and cell lysis, is remarkably robust. A possible explanation  
500 for this difference is that the initial steps of infection rely on low copy-number molecules, such  
501 as one viral genome, or an initial few copies of T7 RNAP, which are subject to large relative  
502 number fluctuations. However, we cannot exclude that variability in the structural properties of  
503 the capsid<sup>45</sup> and consequent attachment to the host cell receptors might contribute to what we  
504 observe. Future studies that quantify the proportion of unsuccessful adsorptions on one side,  
505 and the spatial dynamic of the T7 RNAP within the infected cell, on the other, will help answer  
506 this question.

507  
508 The second phase, in which capsid proteins and, arguably, viable phage particles are  
509 produced within the host cell, exhibits a surprisingly large variability in kinetics and final  
510 amount, despite the robustness in the timing of the events. The strong correlation between  
511 the total protein production and the size of the growth-arrested host suggests that this  
512 variability may originate in physiological differences across infected cells. Indeed, using our  
513 mathematical model, we find that the phage protein production rate strongly depends on the  
514 translational resources of the cell, which scale with cell size, providing a strong mechanistic  
515 link between host cell physiology and phage burst size.

516  
517 Accurate quantification of the sources of phenotypic variability and their relative correlations  
518 across infection events is not only important to understand the underlying molecular  
519 mechanisms controlling phage infection outcomes, but can also have significant evolutionary  
520 consequences. Our simulation results clearly show that mean phenotypic values, such as  
521 average lysis time, are insufficient to predict the fitness advantage of a phage population and  
522 that higher moments of the distribution can have a significant impact. These findings open the  
523 intriguing and currently under-explored possibility that variability in phage phenotype could be  
524 under strong selective pressure<sup>46,47</sup>, raising fascinating questions regarding how evolution  
525 shapes it in different scenarios.

526  
527 Finally, although this work has primarily focused on T7-*E. coli* to benchmark the assay using  
528 a well-studied model system, the approach can readily be applied to any natural, evolved, or  
529 engineered phage. The high-throughput and scalable nature of the platform can be harnessed  
530 for multiplexity, to benchmark a variety of sequence variants of phages against specific target  
531 bacteria or multiple mutants of a target bacteria against a particular phage. Precise  
532 characterisation of properties associated with infection steps (such as adsorption, production,

533 and lysis) can generate a multi-phenotypic profile for each phage-bacteria pair, enabling  
534 detailed analysis of mechanisms underlying response, resistance, and phage-bacteria co-  
535 evolution. Similarly, a collection of natural or engineered phages can be evaluated for their  
536 efficacy in eradicating a target strain, with implications for medical or biotechnological  
537 applications. In summary, this assay promises to open up new avenues for the systems  
538 analysis of phage-bacteria interactions and their practical applications.  
539

## 540 Online Methods

### 541 Bacterial strains and growth conditions

542 The following bacterial strains were used in this study.

543

544 **Table 1: List of *E. coli* strains used in this study**

Name	Species	Genotype	Use
SB8	<i>E. coli</i>	MG1655 7740 $\Delta$ <i>motA</i>	Experiments for Figs. 1 to 6.
SB7	<i>E. coli</i>	SB8- <i>glmS</i> ::PRNA1- mCherry-mKate2	Microfluidic device optimisation experiment (Supplementary note 3), training data for cell segmentation (Supplementary note 4).
BW25113	<i>E. coli</i>	BW25113	Generating phage lysates.

545

546 The motility knockout in SB8 and SB7 prevents cells leaving the trenches of the microfluidic  
547 device. Prior to experiments in the microfluidic device, cells were grown overnight in a shaking  
548 incubator at 250 rpm and 37 °C in LB Miller (Invitrogen) containing 0.8 g L<sup>-1</sup> of pluronic F-108  
549 (Sigma-Aldrich, 542342). Cultures were started directly from a frozen stock to maintain a  
550 consistent genetic diversity across the cells used in experiments across different days. The  
551 LB Miller was sterilised by autoclaving. The pluronic F-108 was first prepared as a 100 g L<sup>-1</sup>  
552 solution and filter sterilised, and then diluted 0.8 % v/v into the LB Miller.

### 553 Phage lysate preparation

554 *E. coli* BW25113 strain cells were grown overnight in a shaking incubator at 250 rpm and 37  
555 °C in LB Miller (Invitrogen). 500 µL of the overnight liquid culture was used to inoculate 20 mL  
556 volume of LB Miller and left to grow in a shaking incubator at 37 °C for 1 h 40 min. Once the  
557 culture reached OD 0.6-0.7, 500 µL of stock phage lysate was added and left in the shaking  
558 incubator for 7 min. The phage-inoculated cells were centrifuged in a pre-chilled (4 °C)  
559 centrifuge at 5000 rpm for 5 min. The supernatant was discarded and the pelleted cells were  
560 resuspended in 2 mL of fresh LB Miller. The resuspended culture was left in the shaking  
561 incubator for 1 h at 37 °C for the infected cells to fully lyse. The lysate was transferred into 1.5  
562 mL Eppendorf tubes and centrifuged at 14000 rpm for 10 min. The resulting supernatant was  
563 passed through 0.22 µm filters to remove any traces of cell debris and unlysed cells.

564

### 565 PFU estimation

566 The number of plaque forming units (PFU) in the filtered lysate was estimated using a plaque  
567 assay. For this, serial dilutions of the filtered lysate were set up ranging from dilution factor  
568 10<sup>5</sup> to 10<sup>8</sup>. 20 µL of each diluted lysate was mixed with 100 µL of overnight BW25113 cells in  
569 5 mL of 0.7% agar LB, kept at 50 °C. The mixture was briefly vortexed and poured as a thin  
570 layer of agar on 9 cm-diameter plates and incubated at 37 °C for 4 h. The formed plaques

571 were counted and the number divided by 20 to estimate the number of PFU per  $\mu\text{L}$  of each  
572 dilution factor. Measurements across three dilution factors were used to estimate the  
573 concentration of PFUs per  $\mu\text{L}$  of the filtered lysate. The titres of lysates obtained using the  
574 above method are listed in Table 2. Filtered lysate was used either directly or stained as per  
575 protocol below. Note that lysate titres listed in Table 2 are diluted into growth media for  
576 microfluidic experiments.

577

578 **Table 2: List of T7 strains and typical corresponding lysate PFUs obtained**

Experiment	Phage strain	Lysate PFU
Figs. 1, 3, 6	T7*, Sytox Orange labelled	$1.0 \times 10^7 \mu\text{L}^{-1}$
Fig. 2	Wild type (WT) T7, Sytox Orange labelled	$3.5 \times 10^7 \mu\text{L}^{-1}$
Fig. 5	WT T7, unlabelled	$4.0 \times 10^7 \mu\text{L}^{-1}$

579

## 580 Genetic engineering of phage: construction of T7\*

581 Transgenic T7 strain T7\* was created by assembling PCR-cloned fragments of WT T7  
582 genome along with the fragment encoding T7 phi10 promoter followed by *E. coli* codon-  
583 optimised mVenus NB (SYFP2) into a circular plasmid. This circularised transgenic genome  
584 was then electroporated into BW25113 cells to produce the transgenic phage lysate. Virions  
585 from individual plaques were isolated and sequenced to establish the isogenic strain of T7\*. A  
586 full description of the PCR protocol to clone the required fragments, the Gibson Assembly of  
587 the transgenic genome, the electroporation protocol and the isolation of transgenic strains is  
588 available in Supplementary note 1.

## 589 Staining the DNA of the phage genome

590 The phage lysate was treated with DNase I-XT to remove any residual bacterial DNA and then  
591 stained with Sytox Orange at the final concentration of 25  $\mu\text{M}$ . Details of the DNase I-XT  
592 treatment and Sytox Orange staining protocol are available in Supplementary note 2.

## 593 Population level measurement of lysis time

594 Population level measurements of the mean lysis time of wild type T7 and T7\* were carried  
595 out according to the 'one-step growth curve' or 'lysis curve' protocol<sup>48</sup>, a full account of which  
596 is available as Supplementary note 12. Measurements were taken in LB using SB8 (Table 1)  
597 as the host bacteria. Each phage's lysis time was measured over three biological replicates,  
598 and we find these values to be  $14.8 \pm 1.3$  min for wild type T7, and  $20.1 \pm 2.0$  min for T7\*  
599 (mean  $\pm$  1 standard error of the mean).

## 600 Microfluidic device fabrication

601 The microfluidic devices were fabricated using soft lithography, by casting a silicone elastomer  
602 onto a silicon wafer. We received this wafer as a gift from Dr. Matthew Cabeen of Oklahoma  
603 State University. It was fabricated by the Searle Clean Room at the University of Chicago  
604 (<https://searle-cleanroom.uchicago.edu/>) according to the specifications provided by Dr.

605 Cabeen and his colleague, Dr. Jin Park. These specifications were based on the design  
606 presented by Norman *et al.*<sup>21</sup>. The silicone elastomer was prepared by mixing  
607 polydimethylsiloxane (PDMS) and curing agent from the Sylgard 184 kit (Dow) in a 5:1 ratio  
608 and degassing for 30 min in a vacuum chamber. The elastomer was then poured onto the  
609 silicon wafer and degassed in a vacuum chamber for a further 1 h. The elastomer was then  
610 cured for 1 h at 95 °C. The appropriate devices were then cut out and inlet and outlet holes  
611 were punched with a 0.75 mm biopsy punch (WPI). Devices were then cleaned with Scotch  
612 Magic tape before being sonicated in isopropanol for 30 min, blow dried with compressed air  
613 and then sonicated in distilled water for 20 min. 22x50 mm glass coverslips (Fisherbrand) were  
614 sonicated for 20 minutes in 1 M potassium hydroxide, rinsed and then sonicated for 20 min in  
615 distilled water before blow drying with compressed air. The devices and coverslips were then  
616 dried for 30 min at 95 °C. Devices and coverslips were plasma bonded using a Diener  
617 Electronic Zepto plasma cleaner, by first pulling a vacuum to 0.1 mbar, and then powering on  
618 the plasma generator at 35% and admitting atmospheric air to a chamber pressure of 0.7 mbar  
619 for 2 min. Device and coverslip were then bonded and heated on a hotplate at 95 °C for 5 min,  
620 before transferring to an oven at 95 °C for 1 h to produce the finished microfluidic devices.

## 621 Single cell infection assay

622 On the day of the experiment, sterile growth media containing LB Miller (Invitrogen) with 0.8 g  
623 L<sup>-1</sup> pluronic F-108 (Sigma-Aldrich) was loaded into a syringe. The pluronic is added as a  
624 surfactant to prevent cell clumping in the overnight culture, to improve cell loading, and to  
625 prevent cells clumping at the outlet of trenches. It is added to the media at sub-inhibitory  
626 concentrations<sup>15</sup>. The lane of the microfluidic device to be loaded was first passivated by  
627 adding the above described growth media into the lane with a gel loading tip, and allowing it  
628 to rest for 10 min. A 1 mL volume of the cells grown overnight were transferred into a 1.5 mL  
629 tube and spun gently at 1000 g for 3 min to sediment the cells. The supernatant was poured  
630 away and the cells resuspended in the residual volume. A small volume of this dense cell  
631 culture was then pushed into the passivated lane using a gel loading tip and left to rest for 10  
632 min. During this time, the small stationary phase cells will diffuse into the trenches.

633  
634 While the cells are diffusing into the trenches, growth media from the syringe is pushed through  
635 a silicone tubing path to purge the tubing of air. The tubing has a forked path, and the flow is  
636 directed down a given fork using a 3-way solenoid pinch valve (Cole Parmer). One fork  
637 supplies the microfluidic device with growth media, while the other leads directly to the waste  
638 bottle.

639  
640 The media flow is then connected to the lane of the device containing the cells using 0.83 mm  
641 outer diameter needles. The outlet flow goes to a waste bottle. Inlet flow from the media  
642 syringe is driven by a syringe pump, and initial flow is set to 100  $\mu\text{L min}^{-1}$  for 10 min to clear  
643 excess cells from the lane. Media flow is then reduced to 5  $\mu\text{L min}^{-1}$ . Following this, 365 nm  
644 illumination light is shone onto the inlet of the device such that each part of the inlet receives  
645 at least 7 min of illumination. This kills any cells not removed by the high flow rate, and helps  
646 to prevent biofilm formation in the device inlet.

647  
648 The cells are grown in the device for a minimum period of 3 h from the introduction of fresh  
649 growth media into the lane, to allow the cells to reach a steady state, exponential growth  
650 phase. After this wake up period, the media is switched to media containing phage to begin

651 the infection imaging. A typical phage media composition is described in Table 3, which would  
652 result in a final phage titre of  $10^6$  PFU  $\mu\text{L}^{-1}$ . Note that the phage lysate is also washed and  
653 resuspended in LB Miller (Supplementary note 2), so the exact lysate volume used is unlikely  
654 to significantly change the nutritional composition of the media.

655

656 **Table 3: Phage treatment media composition**

Component	Volume ( $\mu\text{L}$ )	Volume fraction (-)	Concentration in media
LB Miller	4460	0.892	N/A
Pluronic F-108, 100 $\text{g L}^{-1}$	40	0.008	$0.8 \text{ g L}^{-1}$ pluronic F-108
Phage lysate, PFU $10^7 \mu\text{L}^{-1}$	500	0.100	$10^6$ PFU $\mu\text{L}^{-1}$
<b>Total</b>	5000	1.000	N/A

657

658 The phage titre must be sufficiently high to ensure at least some infections occur in each given  
659 trench, but the exact titre is unimportant in the ranges used, as we operate at very low  
660 multiplicity of infection in order to ensure that all first round infections result from just one  
661 phage binding to a cell. The phage titres used in each experiment are listed in Supplementary  
662 table 6.

663

664 To change the media to phage media, the solenoid pinch valve is activated to block flow to  
665 the microfluidic device. The flow to the microfluidic device is blocked for a maximum of 10 min.  
666 While it is blocked, the growth media syringe is changed to a syringe containing growth media  
667 with phage, and then the tubing is flushed with the phage media at high flow rates, such that  
668 the growth media without phage is completely cleared from the tubing. Then, the flow rate is  
669 returned to  $5 \mu\text{L min}^{-1}$  and the flow is switched to introduce phage media to the cells. Purging  
670 the initial section of tubing with phage media reduces the time between the switch and the  
671 phages reaching the cells, without having to expose the cells to high flow rates which could  
672 cause mechanical stress. Additionally, it purges bubbles which can sometimes be introduced  
673 when the syringes are switched.

674

675 Once the media is switched, time-resolved image acquisition begins.

## 676 Time-resolved image acquisition

677 Images were acquired using a Nikon Eclipse Ti2 inverted microscope with a Hamamatsu  
678 C14440-20UP camera. The microscope has an automated stage and a perfect focus system,  
679 which automatically maintains focus over time. The microscope contains two multiband filter  
680 cubes, each of which contains a multi-bandpass dichroic mirror and corresponding multiband  
681 excitation and emission filters. There is an additional emission filter which can be quickly  
682 switched to select the correct emission wavelength band. Together the multiband cubes and  
683 the emission filter wheel allow for fast imaging in multiple colour channels. All captured images  
684 are initially saved using Nikon's ND2 file format. For the experiments in Figs. 1, 2, 3 and 6,  
685 imaging began before the phage media reached the cells, and continued at a regular  
686 frequency for the duration of the experiments.

687  
688  
689  
690

The microscope settings used for each channel are listed in Table 4 below.

**Table 4: Imaging settings for different experiments used in this paper**

Experiment	Channel	Light source	Filter cube	Emission filter band centre/ band width (nm)	Objective	Imaging interval (s)
Figs. 1, 3, 6	Yellow	514 nm	LED-CFP/YFP/m Cherry-3X3M-A	540/21	Plan Apo $\lambda$ 100x Oil Ph3 DM	30
Figs. 1, 3, 6	Orange	561 nm	LED-DA/FI/TR/C y5-B	595/40	Plan Apo $\lambda$ 100x Oil Ph3 DM	30
Figs. 1, 3, 6	Phase contrast	Köhler	LED-CFP/YFP/m Cherry-3X3M-A	540/21	Plan Apo $\lambda$ 100x Oil Ph3 DM	30
Fig. 2	Orange	561 nm	LED-DA/FI/TR/C y5-B	595/40	Plan Apo $\lambda$ 100x Oil Ph3 DM	10
Fig. 2	Phase contrast	Köhler	LED-DA/FI/TR/C y5-B	515/30	Plan Apo $\lambda$ 100x Oil Ph3 DM	10
Fig. 5	Phase contrast	Köhler	LED-DA/FI/TR/C y5-B	515/30	Plan Apo $\lambda$ 100x Oil Ph3 DM	0.01

691  
692  
693  
694  
695  
696  
697  
698  
699  
700

We have used high-speed timelapse imaging (100 frames s<sup>-1</sup>) to capture the events preceding the lysis, as our initial attempts using 1 frame s<sup>-1</sup> imaging revealed that the structural changes occurring during lysis unfold on sub-second timescales. The high frame rate, while conducive to observing rapid dynamics, renders fluorescence imaging unsuitable due to photobleaching and potential phototoxicity. Nonetheless, phase-contrast imaging is sufficient to gain a detailed insight into the material loss from the cell to its surroundings in the fleeting moments preceding lysis (Fig. 5). A short exposure time (3 ms) and a small region of interest (ROI) around individual trenches enabled us to achieve an imaging interval of 10.2 ms (Supplementary movie 4).

## 701 Image preprocessing

702 All captured images were pre-processed before feature extraction. First, individual frames  
703 from the Nikon ND2 format were extracted and saved as PNG files using custom Python code  
704 which makes use of the nd2 module (<https://pypi.org/project/nd2/>). Using custom Python code  
705 (<https://github.com/georgeoshardo/PyMMM>), these frames were then registered to correct for

706 any stage drift and rotated to ensure the trenches were vertical in the images. We then use  
707 automated methods to find the position of each trench in the images and crop out the trenches  
708 for further processing, as described below.

## 709 Cell segmentation

710 The phase contrast images of cells in the extracted trench images from our experiments in  
711 Figs. 1, 3 and 6 were segmented using a custom trained Omnipose machine learning model<sup>49</sup>.  
712 The model was trained on images (taken on a different day) of SB7 *E. coli* (Table 1) growing  
713 in our device where both fluorescence and phase contrast images were acquired using the  
714 same objective as for the experiments. These images will be referred to as training images,  
715 and are separate from the experiment image data.

716  
717 To train the model, our approach was to first train an Omnipose model to segment  
718 fluorescence images. To generate a high volume of training data and corresponding ground  
719 truth masks for fluorescence images of cells in the mother machine, we use a virtual  
720 microscopy platform called SyMBac<sup>23</sup>. Using this fluorescence model, we segmented  
721 fluorescence images of cells and generated cell masks for the fluorescence channel of the  
722 training images.

723  
724 The cell masks for the fluorescence channel were then checked against the phase contrast  
725 training images, and pairs of fluorescence masks and phase contrast training images which  
726 matched well were manually curated into a training data set. This training data was used to  
727 train an Omnipose model for the segmentation of phase contrast images. The phase contrast  
728 model was then used to generate cell masks for the experiment image data. This pipeline is  
729 further described in Supplementary note 4.

## 730 Feature extraction

731 Basic cell properties, such as cell position, length, area, and YFP intensity, were extracted  
732 from regions of the images corresponding to the cell masks produced by segmentation. The  
733 cell properties were extracted using custom Python code  
734 ([https://github.com/CharlieW313/MM\\_regionprops](https://github.com/CharlieW313/MM_regionprops)) utilising the scikit-image regionprops  
735 function<sup>50</sup>. For the data in Fig. 3, further properties are calculated from the basic cell properties.  
736 Mathematical descriptions are found in Supplementary table 7 of Supplementary note 16.

## 737 Single cell lineage tracking

738 The single cell growth and lysis traces were tracked over time using features extracted at each  
739 frame, including cell position, area, orientation, and Zernike moments. This process was done  
740 using a custom Python script (<https://github.com/erezli/MMLineageTracking>). The algorithm  
741 predicts many potential states of these features for each cell at subsequent time steps. It then  
742 finds the best match to the feature states in the following frame to determine the tracking  
743 outcome. The results are stored in tree-structured Python objects containing detailed cell  
744 properties such as YFP mean intensity. The tracking results are manually checked by  
745 visualising them in kymographs. Further information about the algorithm can be found in  
746 Supplementary note 5.

## 747 Single phage tracking

748 To track the injection of the phage genome, we monitored the intensity of the bright spot  
749 indicating the phage location over consecutive frames until injection was complete. Spot  
750 intensity was measured as the mean intensity of a fraction of the brightest pixels in a  
751 rectangular box centred on the spot, with a control box alongside for background comparison.  
752 Genome injection duration was estimated as the time between adsorption and spot intensity  
753 returning to control box levels. Further details concerning the tracking of individual phage spots  
754 and the calculation of genome injection time are presented in Supplementary note 7.

## 755 Analysis of capsid production data

756 The fluorescence intensity in the yellow channel was analysed to determine the start of capsid  
757 production, as the time point where the signal from the YFP reporter of capsid production  
758 increases above the baseline. We subtract the background intensity from the raw total  
759 intensity of the YFP reporter to give a total intensity,  $I(t)$ , as described in Supplementary table  
760 7. The production start time,  $t_3$ , is calculated as the first time point when the total intensity  
761 reaches a threshold value (chosen to be 1420 AU based on inspection of the intensity time-  
762 series), and then subsequently remains above that threshold for a total of four consecutive  
763 time points. This start is later adjusted to  $t_3^*$  by fitting the model, as explained in  
764 Supplementary note 11.

## 765 Analysis of perforation and lysis

766 For the high time resolution imaging of phage induced lysis, a machine learning based  
767 approach for cell segmentation was unsuitable. This was because we wished to monitor the  
768 phase contrast intensity of the cell before, during and after lysis, so any attempt to segment  
769 the cells using features of the image would begin to fail as those features markedly changed  
770 through the lysis process. We therefore used a hand-drawn manual segmentation of a static  
771 region at the location of each cell in Fiji (ImageJ), as the cells did not move significantly over  
772 the short timescales of lysis. The mean phase contrast pixel intensity of this region,  $i_{PC}(t)$ ,  
773 was then measured in each frame. By translating the static region by  $1.43 \mu\text{m}$  to the left and  
774 right of the cell (along the short axis of the trench), the phase contrast intensities of the regions  
775 adjacent to the cell were also measured. By further translating the region on the right of the  
776 cell an additional  $0.72 \mu\text{m}$  to the right and  $4.29 \mu\text{m}$  along the long axis of the trench towards  
777 its closed end, a region in the side trench far away from the lysis was used as a control region  
778 for the phase contrast intensity.

779  
780 To determine the start of perforation ( $t_4$ ), the mean and standard deviation of the phase  
781 contrast intensity over 200 time points (a window ending a few seconds prior to the perforation  
782 start) were computed. The perforation start was declared when the phase contrast intensity  
783 first exceeds this calculated mean plus three standard deviations, for a minimum of five  
784 consecutive time points. The start of lysis ( $t_5$ ) was determined as the point where the phase  
785 contrast intensity sharply increases from the perforation line (indicated by the arrow in Fig.  
786 5d). We refer to the time interval between these two timepoints as the perforation time.

## 787 Serial passage simulations

788 The simulation extends infection kinetic ODEs<sup>41</sup> to a stochastic, agent-based model (for a full  
789 description of the implementation see Supplementary note 14). The simulation begins with 2  
790 pools of 100 phage and 10,000 susceptible bacteria in a simulated well mixed volume of 10<sup>-5</sup>  
791 ml. All bacteria begin the simulation in the ‘uninfected’ state, at random points in their cell  
792 cycle. In each simulation time-step, ‘bacterial growth’, ‘adsorption’, ‘infection’, ‘lysis’, and  
793 ‘decay’ substeps occur.

794  
795 Once the number of cells has dropped below 100, we simulate a ‘bottleneck’: a 1,000 fold  
796 dilution of the phage and remaining cells, and addition of 10,000 new susceptible bacteria.  
797 The simulation continues, with bottlenecks occurring every time the bacterial population falls  
798 below 100, until either one phage pool outnumbers the other 70:30 and is declared the winner,  
799 or until a preset timeout, at which point we declare a tie.

## 800 Acknowledgements

801 We are thankful to the members of the Bakshi Lab and Fusco lab for their support and  
802 feedback on this work.

## 803 Declarations

### 804 Funding

805 The research in the Bakshi lab was supported by the Wellcome Trust Award (grant number  
806 RG89305), a University Startup Award for Lectureship in Synthetic Biology (grant number  
807 NKXY ISSF3/46), an EPSRC New Investigator Award (EP/W032813/1) and a seed fund from  
808 the School of Technology at University of Cambridge. The research in the Fusco lab was  
809 supported by the Department of Physics, University of Cambridge, a Royal Society Research  
810 Grant (RGS\R2\212131) and an ERC Starting Grant/UKRI Horizon Europe Guarantee  
811 (EP/Y030141/1). Charlie Wedd was supported by the UK Engineering and Physical Sciences  
812 Research Council (EPSRC) grant EP/S023046/1 for the EPSRC Centre for Doctoral Training  
813 in Sensor Technologies for a Healthy and Sustainable Future. Georgeos Hardo was supported  
814 by United Kingdom Biotechnology and Biological Sciences (BBSRC) University of Cambridge  
815 Doctoral Training Partnership 2 (BB/M011194/1). Michael Hunter was supported by a UKRI  
816 EPSRC Doctoral Studentship from the Department of Physics, University of Cambridge  
817 (2125180). Simulations in this work were performed using resources provided by the  
818 Cambridge Service for Data Driven Discovery (CSD3) operated by the University of  
819 Cambridge Research Computing Service ([www.csd3.cam.ac.uk](http://www.csd3.cam.ac.uk)), provided by Dell EMC and  
820 Intel using Tier-2 funding from the Engineering and Physical Sciences Research Council  
821 (capital grant EP/T022159/1), and DiRAC funding from the Science and Technology Facilities  
822 Council ([www.dirac.ac.uk](http://www.dirac.ac.uk)).

### 823 Competing interests

824 The authors declare no competing interests.

## 825 Authors' contributions

826 S.B. and D.F. conceived the study and were in charge of the overall direction and planning.  
827 C.W., T.Y., A.S., M.H., D.F., and S.B. designed the experiments and simulations. C.W. carried  
828 out the microfluidics microscopy experiments, A.S. and M.H. carried out the bulk experiments,  
829 and T.Y. carried out the staining and genetic engineering of phages. C.W., R.L., G.H., and S.B.  
830 designed the data analysis pipeline and carried out the data analysis. M.H., A.S., and D.F.  
831 carried out the simulations and associated analysis. D.F. developed the mathematical model  
832 and associated analysis. C.W., D.F., and S.B., lead the manuscript writing. R.M. contributed  
833 experimental material and methods. All the other authors provided critical feedback and  
834 contributed to the manuscript.

## 835 Data availability:

836 Data for this paper is available from the Zenodo repository associated with this paper, which  
837 can be found at [10.5281/zenodo.13227935](https://zenodo.org/record/13227935).

## 838 Code availability:

839 Microscopy images were registered using the custom-built python script:  
840 <https://github.com/georgeoshardo/PyMMM>. Registered images were segmented using an  
841 Omnipose model trained with synthetic image data generated using the SyMBac pipeline:  
842 <https://github.com/georgeoshardo/SyMBac>. Single-cell features from the segmented images  
843 were extracted using [https://github.com/CharlieW313/MM\\_regionprop](https://github.com/CharlieW313/MM_regionprop). The custom-built  
844 Python script for tracking individual cell lineages in time series data is available at:  
845 <https://github.com/erezli/MMLineageTracking>. Python scripts for phage diffusion simulations,  
846 phage competition simulations, and Matlab script for fitting gene-expression data to  
847 mathematical models are available at: <https://github.com/FuscoLab/single-cell-phage-tracking>  
848 .

## 849 References

- 850 1. Campbell, A. The future of bacteriophage biology. *Nat. Rev. Genet.* **4**, 471–477 (2003).
- 851 2. Koskella, B., Hernandez, C. A. & Wheatley, R. M. Understanding the Impacts of  
852 Bacteriophage Viruses: From Laboratory Evolution to Natural Ecosystems. *Annu. Rev.*  
853 *Viol.* **9**, 57–78 (2022).
- 854 3. Schwartz, M. The adsorption of coliphage lambda to its host: Effect of variations in the  
855 surface density of receptor and in phage-receptor affinity. *J. Mol. Biol.* **103**, 521–536 (1976).
- 856 4. Weigel, C. & Seitz, H. Bacteriophage replication modules. *FEMS Microbiol. Rev.* **30**, 321–  
857 381 (2006).
- 858 5. You, L., Suthers, P. F. & Yin, J. Effects of Escherichia coli Physiology on Growth of Phage  
859 T7 In Vivo and In Silico. *J. Bacteriol.* **184**, 1888–1894 (2002).
- 860 6. Davis, K. M. & Isberg, R. R. Defining heterogeneity within bacterial populations via single  
861 cell approaches. *BioEssays* **38**, 782–790 (2016).
- 862 7. Hyman, P. & Abedon, S. T. Practical Methods for Determining Phage Growth Parameters.  
863 in *Bacteriophages: Methods and Protocols, Volume 1: Isolation, Characterization, and*  
864 *Interactions* (eds. Clokie, M. R. J. & Kropinski, A. M.) 175–202 (Humana Press, Totowa,  
865 NJ, 2009).
- 866 8. Kobiler, O. *et al.* Quantitative kinetic analysis of the bacteriophage  $\lambda$  genetic network. *Proc.*  
867 *Natl. Acad. Sci.* **102**, 4470–4475 (2005).
- 868 9. Wolfram-Schauerte, M., Pozhydaieva, N., Viering, M., Glatter, T. & Höfer, K. Integrated  
869 Omics Reveal Time-Resolved Insights into T4 Phage Infection of E. coli on Proteome and  
870 Transcriptome Levels. *Viruses* **14**, 2502 (2022).
- 871 10. Conners, R. *et al.* Cryo-electron microscopy of the f1 filamentous phage reveals  
872 insights into viral infection and assembly. *Nat. Commun.* **14**, 2724 (2023).
- 873 11. Wang, C., Tu, J., Liu, J. & Molineux, I. J. Structural dynamics of bacteriophage P22  
874 infection initiation revealed by cryo-electron tomography. *Nat. Microbiol.* **4**, 1049–1056  
875 (2019).

- 876 12. Golding, I. Single-Cell Studies of Phage  $\lambda$ : Hidden Treasures Under Occam's Rug.  
877 *Annu. Rev. Virol.* **3**, 453–472 (2016).
- 878 13. Kiss, B. *et al.* Imaging the Infection Cycle of T7 at the Single Virion Level. *Int. J. Mol.*  
879 *Sci.* **23**, 11252 (2022).
- 880 14. Attrill, E. L., Łapińska, U., Westra, E. R., Harding, S. V. & Pagliara, S. Slow growing  
881 bacteria survive bacteriophage in isolation. *ISME Commun.* **3**, 1–9 (2023).
- 882 15. Bakshi, S. *et al.* Tracking bacterial lineages in complex and dynamic environments with  
883 applications for growth control and persistence. *Nat. Microbiol.* **6**, 783–791 (2021).
- 884 16. Jack, B. R., Boutz, D. R., Paff, M. L., Smith, B. L. & Wilke, C. O. Transcript degradation  
885 and codon usage regulate gene expression in a lytic phage. *Virus Evol.* **5**, vez055 (2019).
- 886 17. Balleza, E., Kim, J. M. & Cluzel, P. Systematic characterization of maturation time of  
887 fluorescent proteins in living cells. *Nat. Methods* **15**, 47–51 (2018).
- 888 18. Studier, F. W. The genetics and physiology of bacteriophage T7. *Virology* **39**, 562–574  
889 (1969).
- 890 19. Van Valen, D. *et al.* A Single-Molecule Hershey-Chase Experiment. *Curr. Biol.* **22**,  
891 1339–1343 (2012).
- 892 20. Bakshi, S. *et al.* Nonperturbative Imaging of Nucleoid Morphology in Live Bacterial  
893 Cells during an Antimicrobial Peptide Attack. *Appl. Environ. Microbiol.* **80**, 4977–4986  
894 (2014).
- 895 21. Norman, T. M., Lord, N. D., Paulsson, J. & Losick, R. Memory and modularity in cell-  
896 fate decision making. *Nature* **503**, 481–486 (2013).
- 897 22. Wang, P. *et al.* Robust growth of Escherichia coli. *Curr. Biol. CB* **20**, 1099–1103 (2010).
- 898 23. Hardo, G., Noka, M. & Bakshi, S. Synthetic Micrographs of Bacteria (SyMBac) allows  
899 accurate segmentation of bacterial cells using deep neural networks. *BMC Biol.* **20**, 263  
900 (2022).
- 901 24. Chen, W. *et al.* Structural changes in bacteriophage T7 upon receptor-induced genome  
902 ejection. *Proc. Natl. Acad. Sci.* **118**, e2102003118 (2021).
- 903 25. Swanson, N. A. *et al.* Cryo-EM structure of the periplasmic tunnel of T7 DNA-

- 904       ejectosome at 2.7 Å resolution. *Mol. Cell* **81**, 3145–3159.e7 (2021).
- 905   26.    Pao, C.-C. & Speyer, J. F. Order of Injection of T7 Bacteriophage DNA. *J. Virol.* **11**,
- 906       1024–1026 (1973).
- 907   27.    Molineux, I. J. No syringes please, ejection of phage T7 DNA from the virion is enzyme
- 908       driven. *Mol. Microbiol.* **40**, 1–8 (2001).
- 909   28.    Kemp, P., Gupta, M. & Molineux, I. J. Bacteriophage T7 DNA ejection into cells is
- 910       initiated by an enzyme-like mechanism. *Mol. Microbiol.* **53**, 1251–1265 (2004).
- 911   29.    García, L. R. & Molineux, I. J. Rate of translocation of bacteriophage T7 DNA across
- 912       the membranes of *Escherichia coli*. *J. Bacteriol.* **177**, 4066–4076 (1995).
- 913   30.    Proshkin, S., Rahmouni, A. R., Mironov, A. & Nudler, E. Cooperation between
- 914       translating ribosomes and RNA polymerase in transcription elongation. *Science* **328**, 504–
- 915       508 (2010).
- 916   31.    Kiro, R. *et al.* Gene product 0.4 increases bacteriophage T7 competitiveness by
- 917       inhibiting host cell division. *Proc. Natl. Acad. Sci.* **110**, 19549–19554 (2013).
- 918   32.    Molshanski-Mor, S. *et al.* Revealing bacterial targets of growth inhibitors encoded by
- 919       bacteriophage T7. *Proc. Natl. Acad. Sci. U. S. A.* **111**, 18715–18720 (2014).
- 920   33.    Doermann, A. H. The intracellular growth of bacteriophages. I. Liberation of
- 921       intracellular bacteriophage T4 by premature lysis with another phage or with cyanide. *J.*
- 922       *Gen. Physiol.* **35**, 645–656 (1952).
- 923   34.    Abedon, S. T., Herschler, T. D. & Stopar, D. Bacteriophage Latent-Period Evolution as
- 924       a Response to Resource Availability. *Appl. Environ. Microbiol.* **67**, 4233–4241 (2001).
- 925   35.    Wang, I.-N. Lysis timing and bacteriophage fitness. *Genetics* **172**, 17–26 (2006).
- 926   36.    Nguyen, H. M. & Kang, C. Lysis Delay and Burst Shrinkage of Coliphage T7 by
- 927       Deletion of Terminator T $\phi$  Reversed by Deletion of Early Genes. *J. Virol.* **88**, 2107–2115
- 928       (2014).
- 929   37.    Bull, J. J. & Wang, I. -N. Optimality models in the age of experimental evolution and
- 930       genomics. *J. Evol. Biol.* **23**, 1820–1838 (2010).
- 931   38.    Kerr, B., Neuhauser, C., Bohannan, B. J. M. & Dean, A. M. Local migration promotes

- 932 competitive restraint in a host-pathogen ‘tragedy of the commons’. *Nature* **442**, 75–78  
933 (2006).
- 934 39. Heineman, R. H., Bull, J. J. & Hansen, T. Testing Optimality with Experimental  
935 Evolution: Lysis Time in a Bacteriophage. *Evol. Int. J. Org. Evol.* **61**, 1695–1709 (2007).
- 936 40. Kannoly, S., Singh, A. & Dennehy, J. J. An Optimal Lysis Time Maximizes  
937 Bacteriophage Fitness in Quasi-Continuous Culture. *mBio* **13**, e03593-21 (2022).
- 938 41. Yin, J. & McCaskill, J. S. Replication of viruses in a growing plaque: a reaction-diffusion  
939 model. *Biophys. J.* **61**, 1540–1549 (1992).
- 940 42. Fort, J. & Méndez, V. Time-Delayed Spread of Viruses in Growing Plaques. *Phys. Rev.*  
941 *Lett.* **89**, 178101 (2002).
- 942 43. Hunter, M. & Fusco, D. Superinfection exclusion: A viral strategy with short-term  
943 benefits and long-term drawbacks. *PLOS Comput. Biol.* **18**, e1010125 (2022).
- 944 44. Hunter, M., Krishnan, N., Liu, T., Möbius, W. & Fusco, D. Virus-Host Interactions  
945 Shape Viral Dispersal Giving Rise to Distinct Classes of Traveling Waves in Spatial  
946 Expansions. *Phys. Rev. X* **11**, 021066 (2021).
- 947 45. Coshic, K., Maffeo, C., Winogradoff, D. & Aksimentiev, A. The structure and physical  
948 properties of a packaged bacteriophage particle. *Nature* **627**, 905–914 (2024).
- 949 46. Bull, J. J., Heineman, R. H. & Wilke, C. O. The Phenotype-Fitness Map in Experimental  
950 Evolution of Phages. *PLOS ONE* **6**, e27796 (2011).
- 951 47. Dominguez-Mirazo, M., Harris, J. D., Demory, D. & Weitz, J. S. Accounting for cellular-  
952 level variation in lysis: implications for virus–host dynamics. *mBio* **0**, e01376-24 (2024).
- 953 48. Ellis, E. L. & Delbrück, M. The Growth of Bacteriophage. *J. Gen. Physiol.* **22**, 365–384  
954 (1939).
- 955 49. Cutler, K. J. *et al.* Omnipose: a high-precision morphology-independent solution for  
956 bacterial cell segmentation. *Nat. Methods* **19**, 1438–1448 (2022).
- 957 50. Walt, S. van der *et al.* scikit-image: image processing in Python. *PeerJ* **2**, e453 (2014).
- 958 51. Pedro Coelho, L. Mahotas: Open source software for scriptable computer vision. *J.*  
959 *Open Res. Softw.* **1**, 1–7 (2013).

- 960 52. Taheri-Araghi, S. *et al.* Cell-size control and homeostasis in bacteria. *Curr. Biol. CB*  
961 **25**, 385–391 (2015).
- 962 53. Tinevez, J.-Y. *et al.* TrackMate: An open and extensible platform for single-particle  
963 tracking. *Methods* **115**, 80–90 (2017).
- 964 54. Crocker, J. C. & Grier, D. G. Methods of Digital Video Microscopy for Colloidal Studies.  
965 *J. Colloid Interface Sci.* **179**, 298–310 (1996).
- 966 55. Dunn, J. J. & Studier, F. W. Complete nucleotide sequence of bacteriophage T7 DNA  
967 and the locations of T7 genetic elements. *J. Mol. Biol.* **166**, 477–535 (1983).
- 968 56. Steinier, Jean., Termonia, Yves. & Deltour, Jules. Smoothing and differentiation of data  
969 by simplified least square procedure. *Anal. Chem.* **44**, 1906–1909 (1972).
- 970